

A high-resolution wavefront sensing method to investigate the annular Zernike polynomials behaviour in the indoor convective air turbulence in the presence of a 2D temperature gradient

E. Mohammadi Razi, Saifollah Rasouli, M. Dashti & J. J. Niemela

To cite this article: E. Mohammadi Razi, Saifollah Rasouli, M. Dashti & J. J. Niemela (2021) A high-resolution wavefront sensing method to investigate the annular Zernike polynomials behaviour in the indoor convective air turbulence in the presence of a 2D temperature gradient, *Journal of Modern Optics*, 68:18, 994-1001, DOI: [10.1080/09500340.2021.1968051](https://doi.org/10.1080/09500340.2021.1968051)

To link to this article: <https://doi.org/10.1080/09500340.2021.1968051>



Published online: 05 Sep 2021.



Submit your article to this journal [↗](#)



Article views: 125



View related articles [↗](#)



View Crossmark data [↗](#)



Citing articles: 5 View citing articles [↗](#)



A high-resolution wavefront sensing method to investigate the annular Zernike polynomials behaviour in the indoor convective air turbulence in the presence of a 2D temperature gradient

E. Mohammadi Razi ^a, Saifollah Rasouli ^{a,b,c}, M. Dashti^{a,d} and J. J. Niemela^c

^aDepartment of Physics, Institute for Advanced Studies in Basic Sciences (IASBS), Zanjan, Iran; ^bOptics Research Center, Institute for Advanced Studies in Basic Sciences (IASBS), Zanjan, Iran; ^cThe Abdus Salam ICTP, Trieste, Italy; ^dDepartment of Physics, Zanjan Branch, Islamic Azad university, Zanjan, Iran

ABSTRACT

We report on applications of a two-channel moiré deflectometry wavefront sensor in measurements of wavefront aberrations caused by convective air turbulence generated by a 2D temperature gradient (TG). Data of the wavefront sensor are analysed and the aberrated wavefront is reconstructed and expanded versus Zernike annular polynomials. The results show that variances of the Zernike annular coefficients (except the piston aberration) increase with highest temperature relative to ambient temperature. In particular, we found that the variances of X - and Y -tilt aberration coefficients are not equal when the highest temperature is larger than 40°C. This means that the produced turbulence is not isotropic. Plots of the Zernike annular coefficient variances could be divided into three distinct regions with different slopes.

ARTICLE HISTORY

Received 28 December 2020
Accepted 8 August 2021

KEYWORDS





Zernike annular polynomials; wavefront sensing; Moiré patterns; atmospheric turbulence; temperature gradient; image processing

1. Introduction

Atmospheric turbulence can have a significant impact in many areas, including earth-based astronomical observations, air travel, pollution dispersal, etc. Its study can be enhanced using laser-based methods and the evaluation of wavefront distortion, which can be determined through use of Zernike polynomials. In the case of atmospheric turbulence, conventional and Zernike annular polynomials were used by many authors, e.g. Noll [1] and Fried [2], who were the pioneers in this application. The conventional Zernike polynomials are orthogonal in a circle with a unit radius. For annular pupils, e.g. in a conventional Cassegrain telescope in which the central hole in the primary mirror allows a reflected light from the secondary, annular Zernike polynomials are used to determine the wavefront aberrations. Related efforts can be found in the work by Mahajan [3–8] and Roddier [9], who describe an algorithm that simulates atmospherically distorted wavefronts using a Zernike expansion of randomly weighted Karhunen-Loeve functions. Canan [10] and Hu and coworkers [11] expanded further the use of Zernike polynomials for studying atmospheric turbulence. In this paper, we investigate wavefront aberrations

of a plane wave laser beam with an annular cross-section having a diameter of 20 cm, when it passes through a convective air turbulence with different strengths generated with various 2D temperature gradients (TGs). The wavefront aberrations were determined by measuring the annular Zernike polynomials of the wavefront over the annular area having a diameter 18 cm with a spatial resolution of 3.1 mm in real space.

In applying a Kolmogorov model to the atmospheric turbulence it is generally assumed that, in the inertial range, the turbulence is isotropic and homogeneous [12]. This assumption is never precisely correct, as evidenced by statistical analyses of the wavefront phase subject to passing through a turbulent medium [13–22]. This has also led to a number of theoretical works that address such assumptions in the modelling of atmospheric turbulence [23–26]. In this context we were motivated to investigate this anisotropy by means of an evaluation of the Zernike annular coefficient values in the presence of different 2D TG within a controlled indoor convective air turbulence system, through which we pass a light beam. We use a pair of telescopes, face to face in conjunction with a two-channel moiré deflectometry-based

CONTACT E. Mohammadi Razi  e.mohammadi@ub.ac.ir  Department of Physics, Institute for Advanced Studies in Basic Sciences (IASBS), Zanjan 45137-66731, Iran; Saifollah Rasouli  rasouli@iasbs.ac.ir  Department of Physics, Institute for Advanced Studies in Basic Sciences (IASBS), Zanjan 45137-66731, Iran; Optics Research Center, Institute for Advanced Studies in Basic Sciences (IASBS), Zanjan 45137-66731, Iran; The Abdus Salam ICTP, Strada Costiera 11, 34151 Trieste, Italy

wavefront sensor. This arrangement provides a simple method for the wavefront distortion measurements with a considerable high precision and high resolution [27,28]. It should be mentioned that, in a similar arrangement of two telescopes, we have recently reported significant inhomogeneity and anisotropy on the variances of the horizontal and vertical components of the angle of arrival fluctuations on the entrance pupil of the second telescope [19,22] however, the effect of a 2D TG presenting in the path of a beam on its wavefront fluctuations and aberrations have not been investigated yet.

Here, analysing data from the sensor over a given time interval, successive wavefronts of the light beam are reconstructed and expanded to the Zernike annular polynomials, from which Zernike coefficient variances have been calculated for successive wavefronts. In particular, the dependence of these variances on the TGs are explored. We find that the variances of Zernike coefficients (except the piston aberration) increase with TG as measured by the temperature at the heater. In particular, we find that the variances of x - and y -tilt aberration coefficients are not equal when the heater's temperature is larger than 40°C , demonstrating anisotropy in the turbulence.

2. Experiment

A schematic diagram of the experimental set up is shown in Figure 1(a). The setup consists of a laser, a pair of telescopes, a heater, a two-channel moiré-based wavefront sensor, a CMOS camera, and a computer. A 50 mW CW laser beam with wavelength 532 nm passes through an aspheric lens before entering the first telescope, a 14 inch Celestron (Schmidt-Cassegrain). The light beam is expanded and re-collimated after traversing this confocal system. The emerging plane wave then passes through the turbulent medium, and the aberrated wavefront enters through the aperture of the second telescope (Meade 8 inch Lx200 GPS Schmidt-Cassegrain). After the second telescope, the light beam was re-collimated by a 20 cm focal length lens and then split by a beam splitter, with the beams entering a pair of the moiré deflectometers. It is worth mentioning that we have recently used a very simple version of this arrangement without using the wavefront sensor for the study of inhomogeneity and anisotropy of a similar turbulent medium [19].

Vertical TGs were maintained using a flat plane heater with a surface measurement of $50\text{ cm} \times 100\text{ cm}$. Due to the finite length of the heater's surface, a horizontal

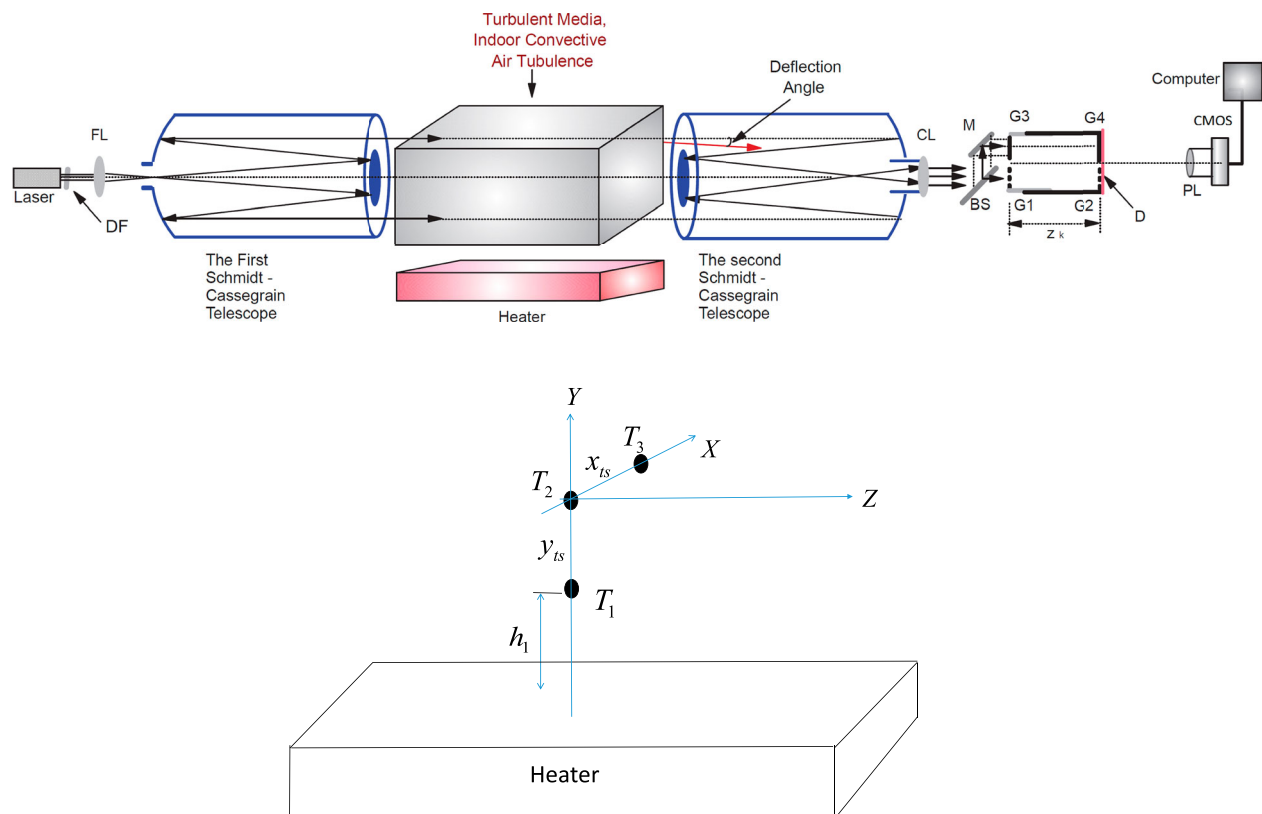


Figure 1. (color online) (a) Schematic diagram of the experimental setup. DF, FL, CL, BS, M, D, and PL stand for the neutral density filter, focusing lens, collimating lens, beam splitter, mirror, and projecting lens, respectively. G1, G2, G3, and G4 stand for the gratings. (b) Locations of the temperature sensors in the turbulent medium. The distances of the central temperature sensor from others are $x_{ts} = y_{ts} = 16.5\text{ cm}$. h_1 is the distance between the location of the lower thermometer (T_1) and the surface of the heater.

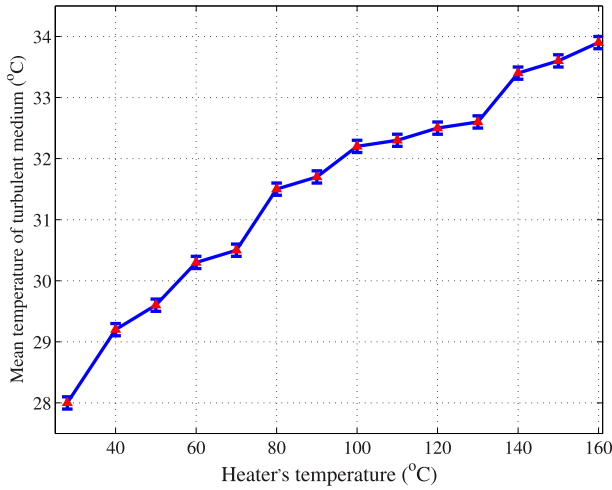


Figure 2. (color online) Mean temperatures of the turbulent medium at a distance of 86 cm from the heater's surface versus the heater's surface temperature.

component of the TG also appears. Figure 1(b) shows how the thermometers used to measure TGs were installed. The sampling rate of the thermometers and their measurement accuracy were 0.33 sample/s and 0.1°C, respectively. The distance of the central sensor (T_2) from the others located in the bottom and side was 16.5 cm. According to the data collected by the sensors, the TGs in the vertical and horizontal directions are not equal. The heater's temperature can be changed from room temperature to 200°C with a fluctuation less than 1°C in steady state. For all data, the vertical distance of the telescopes from the heater was 80 cm. The turbulence medium was isolated from the other parts of the lab with two plastic isolators. The mean value of the turbulent medium temperature at the distance 86 cm from the heater is shown in Figure 2. The temperature fluctuations and fluctuations of the TGs in two directions, at two distances from the heater's surface for two different heater's temperatures are also shown in Figure 3. As it is shown in Figure 3, the temperature of the turbulent medium is higher at the distances are closer to the heater. In addition, the temperature of the turbulent medium decreases when we close to the sides of the medium. Using the temperature fluctuation illustrated in Figure 3(a),(c),(e) the corresponding fluctuations of the TG in two directions, parallel and perpendicular to the heater's surface are calculated and illustrated in (Figure 3(b),(d),(f)). According, the TGs in x and y directions, are different from each other. In other words, we can say that a 2D TG was generated and it causes a convective air turbulence in the medium.

The moiré deflectometers are installed relatively close to each other. The directions of the gratings' rulings are almost parallel in each moiré deflectometer but are perpendicular in the two beams. The second set

of gratings of the moiré deflectometers and a diffuser are located in the plane where the moiré patterns are formed. Successive moiré patterns were recorded by a CMOS (DCC1545 M-high resolution USB2.0 CMOS Monochrome camera) and then were transmitted to a computer. For these measurements the grating period, self-imaging distance, CMOS camera sampling rate, and exposure time, were 0.1 mm, 37.5 mm, 30 frame per second, and 1 ms, respectively. We have recorded many sets of data at different values of the heater temperature. At a given heater temperature, we have recorded at least five sets of data. Each data set was consisted of 2000 frames collected in 66 s. The telescopes were mounted on suitable bases in order to minimize vibrational noise coming from mechanical modes.

3. Wavefront reconstruction and expansion in Zernike annular polynomials

Details of the wavefront reconstruction using a moiré-based wavefront sensor in conjunction with the use of a telescope were reported in [27]. Here we recall a few salient points. Briefly, the aberrated wavefront with a local angle of arrival (AA), α , enters the second telescope aperture of diameter D . On the image plane, the wavefront diameter is $D' = \gamma D$ and the corresponding AA becomes $\alpha' = \frac{\alpha}{\gamma}$, where γ is the magnification of the optical system and is given by $\gamma = \frac{f'}{f}$, and f and f' are the focal lengths of the second telescope and collimating lens, respectively. Components of α' in x and y directions (perpendicular to the gratings' rulings) are given in [29]:

$$[\alpha'_x, \alpha'_y] = \frac{d}{Z_k} \left[\frac{\Delta y_m}{d'_m}, \frac{\Delta x_m}{d_m} \right] \quad (1)$$

where d_m and d'_m are the moiré fringe spacings, Z_k denotes the k th Talbot distance and Δx_m and Δy_m are the moiré fringe shifts in the first and second channels, respectively.

Using $\alpha = \gamma \alpha'$ we obtain

$$[\alpha_x, \alpha_y] = \frac{f'}{f} \frac{d}{Z_k} \left[\frac{\Delta y_m}{d'_m}, \frac{\Delta x_m}{d_m} \right], \quad (2)$$

Since α_x and α_y are equal to the incident wavefront gradients in the x- and y-direction, respectively, the incident wavefront gradients at a given point are determined by

$$\left[\frac{\partial \Phi}{\partial x}, \frac{\partial \Phi}{\partial y} \right] = \frac{f'}{f} \frac{d}{Z_k} \left[\frac{\Delta y_m}{d'_m}, \frac{\Delta x_m}{d'_m} \right]. \quad (3)$$

Using the Hudgin algorithm [30] we have reconstructed wavefronts from the wavefront gradients. In these experiments, 1677 intersection points out of an array of 55×55 points were used for wavefront reconstruction. The

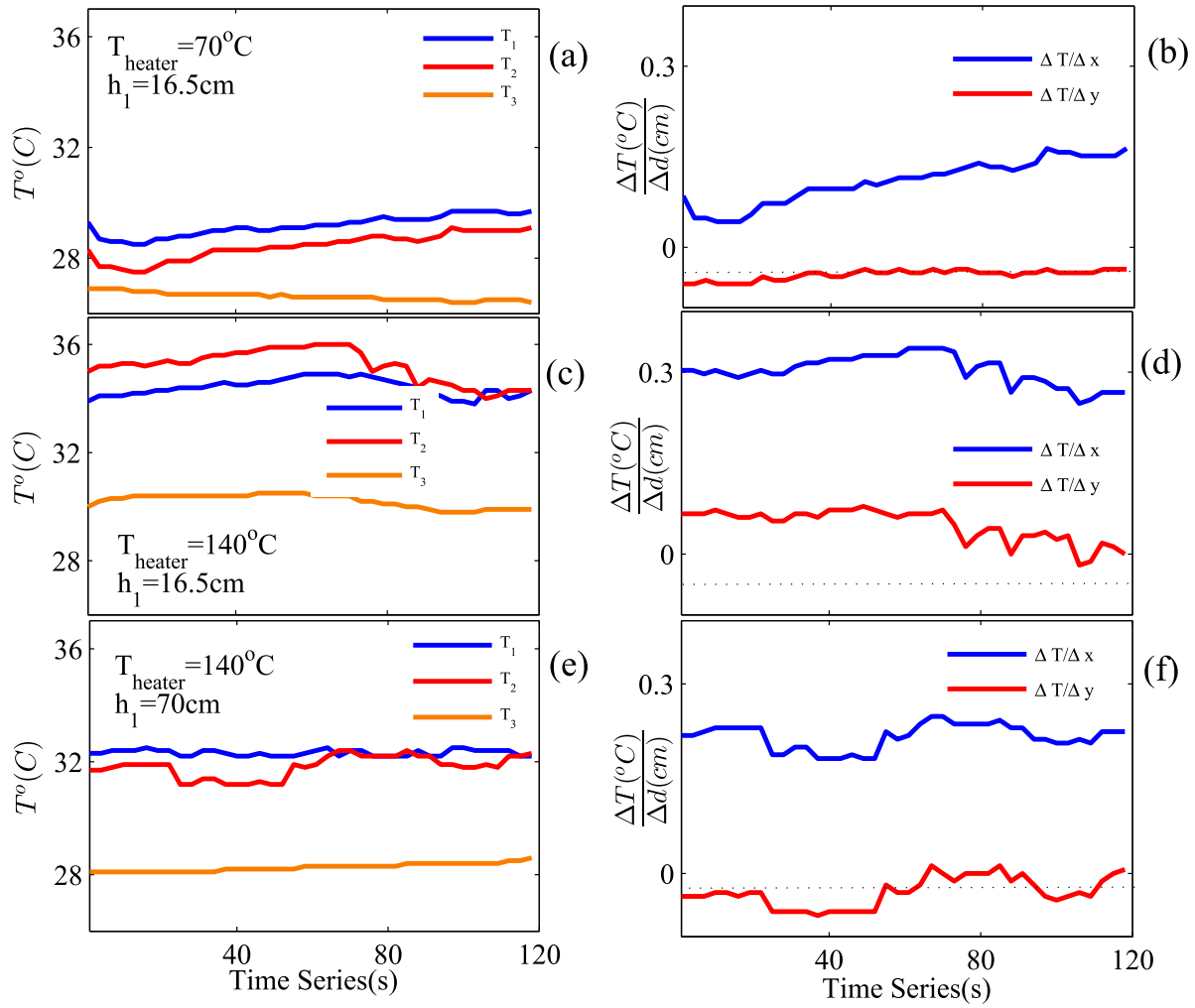


Figure 3. (color online) Time series of temperature fluctuations in (a) heater's temperature of 70°C and at a distance of $h_1 = 16.5\text{ cm}$ from the heater (c) heater's temperature of 140°C and at a distance of $h_1 = 16.5\text{ cm}$ from the heater (e) heater's temperature of 140°C and at a distance of $h_1 = 70\text{ cm}$ from the heater. Corresponding time series of the TG fluctuations in two directions are plotted in (b), (d), and (f).

distance between two adjacent intersection points corresponds to 3.1 mm in real space on the second telescope's aperture plane. It is worth mentioning that, this spatial resolution is high compared to the common Shack-Hartmann wavefront sensors used with about 20×20 lenslet array. In Figure 4(a), typical recorded frames of the moiré patterns corresponding to different heater temperatures are shown.

After reconstruction of the wavefront, it is expanded in ortho-normal Zernike annular polynomials as [4]

$$\Phi(\rho, \theta; \epsilon) = \sum_{j=1} a_j(\epsilon) Z_j(\rho, \theta; \epsilon), \quad (4)$$

where the index j denotes the orders the polynomials and $a_j(\epsilon)$ are the expansion coefficients. The radial variable ρ normalized by the outer radii of entrance pupil of the second telescope. The inner and outer radii of the pupil are ϵ and $\frac{D}{2}$, respectively, in which $\epsilon \leq \rho < 1$ and $0 \leq$

$\theta < 2\pi$. The polynomials may be written as

$$Z_j(\rho, \theta; \epsilon) = \sqrt{n+1} R_n^m(\rho; \epsilon) \Theta^m(\theta), \quad (5)$$

where the $R_n^m(\rho; \epsilon)$ and $\Theta^m(\theta)$ are the annular radial polynomials and triangular function

$$\Theta^m(\theta) = \begin{cases} \sqrt{2} \cos(m\theta) & m \neq 0 \text{ even } j \\ \sqrt{2} \sin(m\theta) & m \neq 0 \text{ odd } j \\ 1 & m = 0 \end{cases}, \quad (6)$$

Indexes n and m are referred to the radial degree and the azimuthal frequency, respectively. Moreover, $n - m \geq 0$. Some of the Zernike annular polynomials are introduced in Table 1. Figure 4(b) shows the corresponding reconstructed wavefront maps of the moiré patterns given in Figure 4(a). Figure 4(c)–(e) shows the corresponding tip and tilt removed residual wavefront maps, the residual wavefront maps after removing the first 14 aberrations,

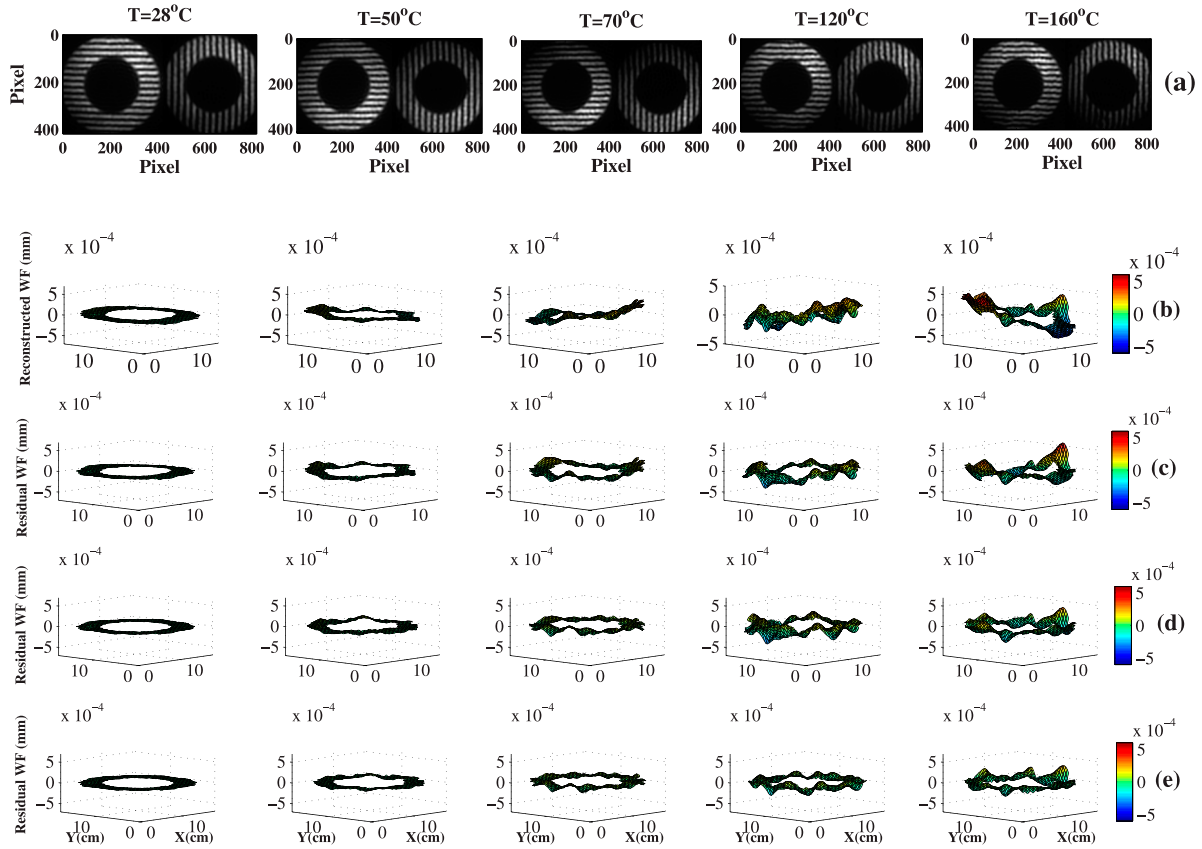


Figure 4. (color online) (a) Typical recorded frame of moiré patterns in different heater's temperature, (b) corresponding reconstructed wavefront maps, (c) the corresponding tip and tilt removed residual wavefront maps, (d) the corresponding residual wavefront maps after removing the first 14 aberrations, and (e) the corresponding residual wavefront maps after removing the first 28 aberrations.

Table 1. Ten orthonormal annular polynomials $Z_j(\rho, \theta; \epsilon)$ with annular pupil of ϵ inner radii.

j	n	m	$Z_j(\rho, \theta; \epsilon)$	Aberration
1	0	0	1	<i>piston</i>
2	1	1	$[2\rho/(1 + \epsilon^2)^{1/2}] \cos \theta$	<i>x tilt</i>
3	1	1	$[2\rho/(1 + \epsilon^2)^{1/2}] \sin \theta$	<i>y tilt</i>
4	2	0	$\sqrt{3}(2\rho^2 - 1 - \epsilon^2)/(1 - \epsilon^2)$	Defocus
5	2	2	$[\sqrt{6}\rho^2/(1 + \epsilon^2 + \epsilon^4)^{1/2}] \sin 2\theta$	45° primary astigmatism
6	2	2	$[\sqrt{6}\rho^2/(1 + \epsilon^2 + \epsilon^4)^{1/2}] \cos 2\theta$	0° primary astigmatism
7	3	1	$\sqrt{8} \frac{3(1+\epsilon^2)\rho^3 - 2(1+\epsilon^2+\epsilon^4)\rho}{(1-\epsilon^2)[(1+\epsilon^2)(1+4\epsilon^2+\epsilon^4)]^{1/2}} \sin \theta$	primary <i>y</i> comma
8	3	1	$\sqrt{8} \frac{3(1+\epsilon^2)\rho^3 - 2(1+\epsilon^2+\epsilon^4)\rho}{(1-\epsilon^2)[(1+\epsilon^2)(1+4\epsilon^2+\epsilon^4)]^{1/2}} \cos \theta$	primary <i>x</i> comma
9	3	3	$[\sqrt{8}\rho^3/(1 + \epsilon^2 + \epsilon^4 + \epsilon^6)^{1/2}] \sin 3\theta$	<i>y</i> trefoil
10	3	3	$[\sqrt{8}\rho^3/(1 + \epsilon^2 + \epsilon^4 + \epsilon^6)^{1/2}] \cos 3\theta$	<i>x</i> trefoil

and the residual wavefront maps after removing the first 28 aberrations, respectively.

Coefficient variances, corresponding to the first nine terms of the Zernike annular polynomial, are plotted against heater temperature in Figure 5. In this work, statistical error of variance of the expansion coefficient measurements was calculated from [31]

$$\delta\sigma_{a_j, \epsilon}^2 = \sqrt{\frac{2}{N-1}} \sigma_{a_j, \epsilon}^2, \quad (7)$$

where $N = 10,000$ is the number of data and $\sigma_{a_j, \epsilon}^2$ is the variance of expansion coefficient. In Figure 6(a), experimental data of variance of Zernike annular coefficients are plotted for different heater's temperatures. As it can be seen from the figure, lower orders of Zernike annular polynomials play important roles in the wavefront's fluctuations. In [7], Mahajan et al. presuming Kolmogorov turbulence, the expected relative strengths of the Zernike annular modes versus the inner radii of annular pupil, were theoretically calculated. Figure 6(b) shows a comparison between the experimental results at the heater's temperature of 150°C, $\epsilon = 0.56$ and the theoretical results for $\epsilon = 0.5$. Comparing Figure 6(a) and (b), it can be seen that the behaviour of the theoretical and the experimental results are the same. However, the theoretical and experimental values of the coefficients' variances do not match. In [32], the authors showed that the same convective air turbulence is a non-Kolmogorov turbulence. This mismatch between the experimental and theoretical results, can be attributed to the non-Kolmogorov behaviour of the turbulence.

In Figure 5, we see that all of the Zernike annular coefficient variances increase as the heater's temperature

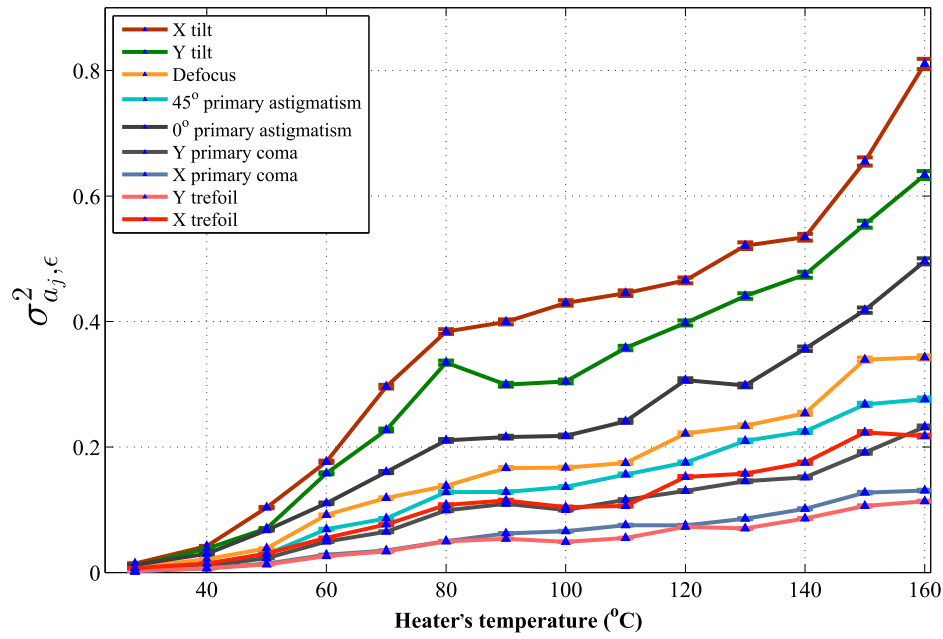


Figure 5. (color online) Primary aberration coefficient variance versus heater temperature.

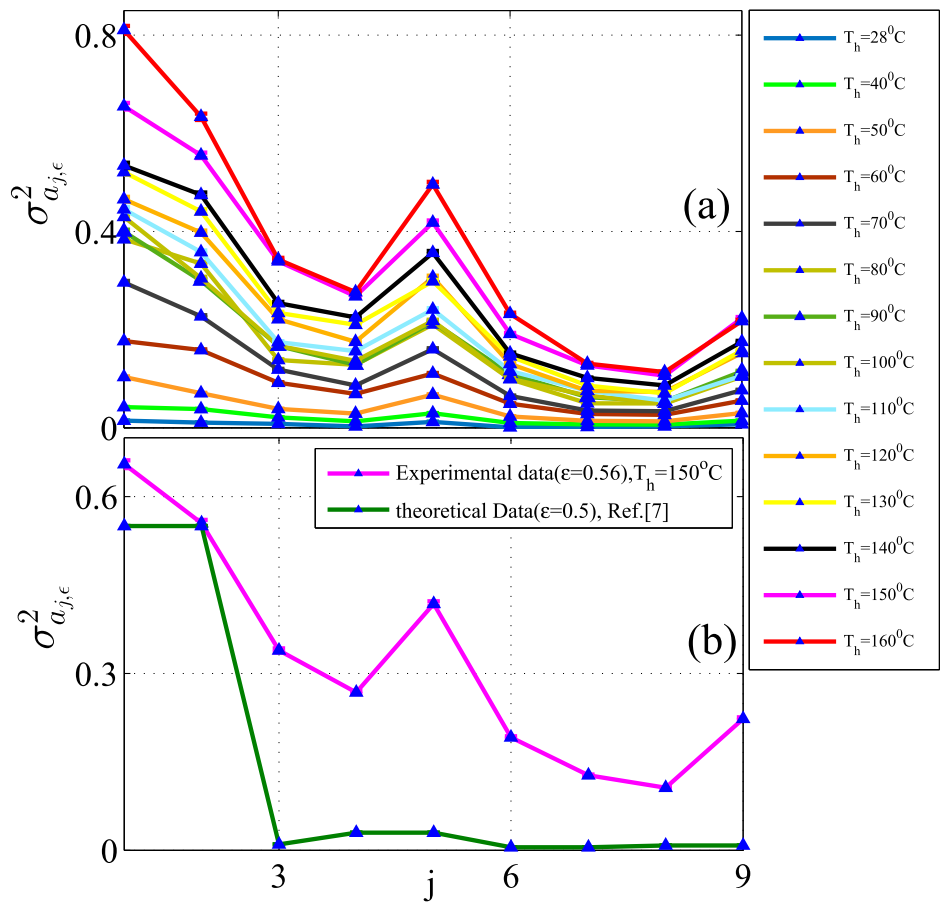


Figure 6. (color online) (a) experimental data of variance of Zernike annular coefficients for different heater's temperature (b) Comparison between the experimental results at heater's temperature of 150°C, $\epsilon = 0.56$ and the theoretical results for $\epsilon = 0.5$.

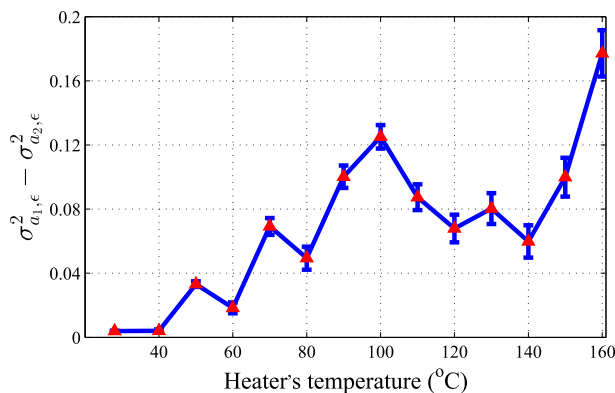


Figure 7. (color online) The difference of the absolute magnitudes of the X- and Y-tilt aberration coefficient variances versus the heater temperature. a_1 and a_2 are the X- and Y-tilt aberration coefficient, respectively. Here again we have $\epsilon = 0.56$.

increases. In addition, the Zernike annular coefficient variances corresponding to the X- and Y-tilt aberrations are not equal when the heater's temperature exceed 40°C . This means that the turbulence is anisotropic. As it can be seen from the figure, the increasing behaviour of the Zernike coefficients can be divided into three regions with different slopes. For the heater's temperature less than 80°C the slopes of the plots are almost considerable. The area between the heater's temperatures of $80 - 140^\circ\text{C}$ can be considered as the second region. The third region starts from 140°C where the plots are smooth and their slopes are larger. At all heater's temperatures, $\sigma_{a_1, \epsilon}^2 > \sigma_{a_2, \epsilon}^2$, thus the difference of the absolute magnitudes of the X- and Y-tilt aberration coefficient variances is almost positive, $\sigma_{a_1, \epsilon}^2 - \sigma_{a_2, \epsilon}^2 > 0$.

For better visualization of the difference between the X- and Y-tilt aberration coefficients, the difference of their respective variances is plotted against heater temperature in Figure 7. It is obvious that the anisotropy is negligible when the heater turns off. But in the presence of a TG with heater temperature greater than 40°C we observe a significant anisotropy. The anisotropy increases as the heater's temperature increases although not monotonically.

As mentioned above the increase of the Zernike coefficients variances can be divided into three regions with different slopes, consequently, the plot of Figure 7 can be also divided into three regions. The physical reasons of both of the observations are under investigation.

4. Conclusion

In this work, we observe for the first time the effect of a 2D TG on the change of the Zernike coefficients of a light beam wavefront after propagating through a controlled turbulent medium. Due to the limited width of heater's

surface, a horizontal component of the TG also appeared. Using a second telescope and a two-channel moiré-based wavefront sensor, the wavefront of the light beam was reconstructed. The reconstructed wavefront was then expanded versus the Zernike annular polynomials. The experiments were performed at different heater temperatures, from room temperature to 160°C . Results show that the variance of the Zernike coefficients increase as the heater temperature increases. Finally, we find that the X- and Y-tilt aberrations coefficient variances are not equal when the heater's temperature exceeds 40°C , suggesting that the convective air turbulence is not isotropic; in particular, plots of the difference in coefficient variance between X- and Y-tilts show non-monotonic increase with heater temperature and can be divided into three distinct regions with different slopes.

Disclosure statement

No potential conflict of interest was reported by the author(s).

ORCID

E. Mohammadi Razi  <http://orcid.org/0000-0002-8250-9980>
 Saifollah Rasouli  <http://orcid.org/0000-0003-2703-8925>

References

- [1] Noll RJ. Zernike polynomials and atmospheric turbulence. *J Opt Soc Am.* **1976**;66:207–211.
- [2] Fried DL. Statistics of a geometric representation of wavefront distortion. *J Opt Soc Am.* **1965**;55:1427–1435.
- [3] Mahajan VN. Zernike annular polynomials for imaging systems with annular pupils. *J Opt Soc Am.* **1981**;71:75–86.
- [4] Mahajan VN. Zernike annular polynomials for imaging systems with annular pupils: errata. *J Opt Soc Am.* **1981**;71:1408.
- [5] Mahajan VN. Zernike annular polynomials for imaging systems with annular pupils. *J Opt Soc Am A.* **1984**;1:685.
- [6] Mahajan VN. Zernike annular polynomials and optical aberrations of system with annular pupils. *Appl Opt.* **1994**;33:8125–8127.
- [7] Dai G-M, Mahajan VN. Zernike annular polynomials and atmospheric turbulence. *J Opt Soc Am A.* **2007**;1:139–159.
- [8] Mahajan VN, Diaz JA. Imaging characteristics of Zernike and annular polynomial aberration. *Appl Opt.* **2013**;52:2062–2074.
- [9] Roddier N. Atmospheric wavefront simulation using Zernike polynomials. *Proc SPIE.* **1990**;29(10):1174–1180.
- [10] Conan R. Mean-square residual error of a wavefront after propagation through atmospheric turbulence and after correction with Zernike polynomials. *J Opt Soc Am.* **2008**;25:526–536.
- [11] Hu PH, Stone J, Stanley T. Investigated the application of Zernike polynomials to atmospheric propagation problems. *J Opt Soc Am.* **1989**;6:1595–1608.

- [12] Kolmogorov AN. Local structure of turbulence in incompressible fluid with very high Reynold's number. *Dokl Akad Nauk SSSR*. 1941;30:301–305.
- [13] Dayton D, Pierson B, Spielbusch B, et al. Atmospheric structure function measurements with a Shack-Hartmann wavefront sensor. *Opt Lett*. 1992;17:1737–1739.
- [14] Nicholls TW, Boreman GD, Dainty JC. Use of a Shack-Hartmann wavefront sensor to measure deviations from a Kolmogorov phase spectrum. *Opt Lett*. 1995;20:2460–2462.
- [15] Lukin VP. Investigation of the anisotropy of the atmospheric turbulence spectrum in the low frequency range. *Proc SPIE*. 1995;2471:347–354.
- [16] Gurvich AS, Belenkii MS. Influence of stratospheric turbulence on infrared imaging. *J Opt Soc Am A*. 1995;12:2517–2522.
- [17] Golbraikh E, Kopeika NS. Behavior of structure function of refraction coefficients in different turbulent fields. *Appl Opt*. 2004;43:6151–6156.
- [18] Rasouli S, Niray MD, Rajabi Y, et al. Applications of 2D Moiré deflectometry to atmospheric turbulence. *J Appl Fluid Mech (JAFM)*. 2014;7(4):651–657.
- [19] Mohammady Razi E, Rasouli S. Measuring significant inhomogeneity and anisotropy in indoor convective air turbulence in the presence of 2D temperature gradient. *J Opt*. 2014;16:045705.
- [20] Rasouli S, Rajabi Y. Investigation of the inhomogeneity of atmospheric turbulence at day and night times. *Opt Laser Technol*. 2016;77:44.
- [21] Wang F, Toselli I, Li J, et al. Measuring anisotropy ellipse of atmospheric turbulence by intensity correlations of laser light. *Opt Lett*. 2017;42(6):1129.
- [22] Razi E, Rasouli S. Impacts of the source temperature and its distance on the statistical behavior of the convective air turbulence. *Appl Phys B*. 2019;125:185.
- [23] Rao Gudimetla VS, Holmes RB, Smith G, et al. Analytical expressions for the log-amplitude correlation function of a plane wave through anisotropic atmospheric refractive turbulence. *J Opt Soc Am A*. 2012;29(5):832.
- [24] Toselli I, Korotkova O. General scale-dependent anisotropic turbulence and its impact on free space optical communication system performance. *J Opt Soc Am A*. 2015;32(6):1017.
- [25] Yao M, Toselli I, Korotkova O. Propagation of electromagnetic stochastic beams in anisotropic turbulence. *Opt Exp*. 2014;23:31608.
- [26] Xiao X, Voelz DG, Toselli I, et al. Gaussian beam propagation in anisotropic turbulence along horizontal links: theory, simulation and laboratory implementation. *Appl Opt*. 2016;55:4079.
- [27] Dashti M, Rasouli S. Measurement and statistical analysis of the wavefront distortions induced by atmospheric turbulence using two-channel Moiré deflectometry. *J Opt*. 2012;14:095704.
- [28] Rasouli S. Use of a Moiré deflectometer on a telescope for atmospheric turbulence measurements. *Opt Lett*. 2010;35:1470.
- [29] Rasouli S, Dashti M, Ramaprakash AN. An adjustable, high sensitivity, wide dynamic range two channel wavefront sensor based on Moiré deflectometry. *Opt Express*. 2010;18:23906.
- [30] Hudgin RH. Wave-front reconstruction for compensated imaging. *J Opt Soc Am*. 1977;67:375.
- [31] Taylor JR. An introduction to error analysis. Sausalito, CA: University Science Books; 1997.
- [32] Rasouli S, Mohammadi RE, Neimela JJ. Investigation of the anisotropy and scaling of the phase structure function in convective air turbulence. to be submitted; 2021.